Reflectivity and Liquid Water Content Vertical Decomposition Diagrams to Diagnose Vertical Evolution of Raindrop Size Distributions

CHRISTOPHER R. WILLIAMS

Cooperative Institute for Research in Environmental Sciences, University of Colorado Boulder, and NOAA/Earth System Research Laboratory, Boulder, Colorado

(Manuscript received 11 October 2015, in final form 30 December 2015)

ABSTRACT

This study consists of two parts. The first part describes the way in which vertical air motions and raindrop size distributions (DSDs) were retrieved from 449-MHz and 2.835-GHz (UHF and S band) vertically pointing radars (VPRs) deployed side by side during the Midlatitude Continental Convective Clouds Experiment (MC3E) held in northern Oklahoma. The 449-MHz VPR can measure both vertical air motion and raindrop motion. The S-band VPR can measure only raindrop motion. These differences in VPR sensitivities facilitates the identification of two peaks in 449-MHz VPR reflectivity-weighted Doppler velocity spectra and the retrieval of vertical air motion and DSD parameters from near the surface to just below the melting layer.

The second part of this study used the retrieved DSD parameters to decompose reflectivity and liquid water content (LWC) into two terms, one representing number concentration and the other representing DSD shape. Reflectivity and LWC vertical decomposition diagrams (Z-VDDs and LWC-VDDs, respectively) are introduced to highlight interactions between raindrop number and DSD shape in the vertical column. Analysis of Z-VDDs provides indirect measure of microphysical processes through radar reflectivity. Analysis of LWC-VDDs provides direct investigation of microphysical processes in the vertical column, including net raindrop evaporation or accretion and net raindrop breakup or coalescence. During a stratiform rain event (20 May 2011), LWC-VDDs exhibited signatures of net evaporation and net raindrop coalescence as the raindrops fell a distance of 2 km under a well-defined radar bright band. The LWC-VDD is a tool to characterize rain microphysics with quantities related to number-controlled and size-controlled processes.

1. Introduction

The Midlatitude Continental Convective Clouds Experiment (MC3E), a 2-month field campaign from mid-April to early-June 2011, had the overarching goal of characterizing convective cloud systems, precipitation, and their environment to improve model cumulus parameterization and satellite-based rainfall retrieval algorithms (Jensen et al. 2016). The deployment of radars, disdrometers, aircraft, and an extensive sounding network (Jensen et al. 2015) during the focused MC3E field campaign provided new, unique, and complementary observations not available from the permanent instruments stationed at the U.S. Department of Energy (DOE) Atmospheric Radiation Measurement (ARM) Southern Great Plains (SGP) Climate Research Facility (Mather and Voyles 2013). Supported by the NASA Precipitation Measurement Mission (PMM) Ground Validation (GV) program (Hou et al. 2014), NOAA deployed vertically pointing radars (VPRs) operating at 449 MHz [ultrahigh-frequency (UHF) band] and 2.835 GHz (S band) to simultaneously observe vertical air motion and hydrometeor motion in precipitating cloud systems (Williams et al. 2007).

The first part of this study builds on the long history of using "clear air" VHF- and UHF-band wind profilers operating at 50, 449, and 915 MHz to estimate and study vertical air motions from Bragg scattering processes (e.g., Balsley and Gage 1982; Gage 1990). VHF- and UHF-band radars are also sensitive to Rayleigh scattering from backscattered energy from raindrops (Fukao et al. 1985). Recording both air and raindrop motions in the same reflectivity-weighted Doppler velocity spectrum enables retrieval algorithms to estimate both vertical air motion and raindrop size distributions (DSDs) from a single Doppler spectrum (Wakasugi et al. 1986; Rajopadhyaya et al. 1998). Since backscattered

Corresponding author address: Christopher R. Williams, Cooperative Institute for Research in Environmental Sciences, University of Colorado Boulder, 216 UCB, Boulder, CO 80309-0216.
E-mail: christopher.williams@colorado.edu

DOI: 10.1175/JTECH-D-15-0208.1

energy due to Bragg scattering decreases as radar operating frequency increases (Ecklund et al. 1995), air motion peaks in 449- and 915-MHz VPR spectra are much smaller than raindrop motion peaks. The smaller air motion peaks make it difficult for retrieval algorithms to identify and isolate the two spectral peaks appearing in the same spectrum (Kanofsky and Chilson 2008). To help detect and isolate weak air motion signals in the 449-MHz VPR spectra, NOAA deployed an S-band VPR that is sensitive only to raindrop Rayleigh scattering. Using a dual-frequency retrieval technique (Williams 2012a), the first part of this study combines 449-MHz and S-band VPR spectra to estimate vertical air motion and DSDs in the vertical column.

The second part of this study uses the 449-MHz and S-band VPR-retrieved DSDs to study DSD vertical structure and evolution. Although a three-parameter gamma shape DSD may not represent measurements made with small sample volumes or short durations (Ignaccolo and De Michele 2014; Adirosi et al. 2015; Ekerete et al. 2015), it is beneficial to model DSDs with gamma shapes because numerical models often parameterize microphysical processes assuming gamma-shaped DSDs (Morrison et al. 2012). Vertical profiles of DSD parameters were retrieved from VPR spectra modeled with normalized raindrop number concentration N_w ($\mathrm{mm}^{-1}\,\mathrm{m}^{-3}$), mass-weighted mean diameter D_m (mm), and gamma distribution shape parameter μ (unitless) (Testud et al. 2001; Illingworth and Blackman 2002; Bringi et al. 2003).

From a radar measurement perspective, the vertical structure of precipitation can be examined using reflectivity and vertical profiles of N_w and D_m (or D_0, which is the mass spectrum median diameter) (Bringi et al. 2015). Because of differences in standard units of measurement (i.e., reflectivity is often represented in logarithmic units and DSD parameters are represented in linear units), it can be difficult to quantify the way in which changes in reflectivity are related to changes in either N_w or D_m. To address this difficulty, this study decomposes reflectivity into two terms expressed in logarithmic units with one term determined by the normalized number concentration and the other determined by the size and breadth of the DSD. One benefit of expressing quantities in logarithmic units is that a change of 1, 2, or 3 dB corresponds to a relative change of 26%, 58%, or 100%, respectively.

Although decomposing reflectivity into two terms is helpful for interpreting radar measurements with height, decomposing reflectivity does not directly measure evaporation, breakup, or coalescence processes of falling raindrops. These processes could be better assessed if DSD attributes were expressed in the liquid water content (LWC) domain.

Following the reflectivity decomposition logic, LWC is first estimated from the VPR-retrieved DSDs and then decomposed into two logarithmic terms: one representing raindrop total number concentration and another representing mass-weighted raindrop size and breadth. This decomposition in the LWC domain and the development of the LWC vertical decomposition diagram (LWC-VDD) allows for a qualitative analysis of evaporation, as well as breakup and coalescence processes in the vertical column. This decomposition enables microphysical processes to be studied with regard to number-controlled or size-controlled conditions as described in Steiner et al. (2004).

This paper has the following structure. Section 2 describes the NOAA 449-MHz and S-band VPRs deployed during MC3E and their calibration using surface disdrometer observations for the 20 May 2011 rain event. Section 3 describes the methods used to retrieve air motion and DSD parameters from VPR Doppler velocity spectra. Sections 4 and 5 describe the mathematics of reflectivity and LWC decompositions, respectively, along with observations from 20 May 2011. Conclusions are presented in section 6.

2. NOAA VPRs deployed during MC3E

During MC3E, seven radars were deployed at the DOE ARM SGP central facility in northern Oklahoma. Figure 1 shows photographs of the radars with views to the west (Fig. 1a) and to the east (Fig. 1b). The NOAA 449-MHz VPR (operating in the UHF band) used an 8-m square phased array antenna (see Fig. 1) to form a 9° radar beam continuously pointed in the vertical direction. Using the radar operating parameters listed in Table 1, it took approximately 45 s to collect 360 448 radar pulses, which were processed to produce a Doppler velocity spectrum at every range gate. Because of leakage through the transmit-and-receive switch, noise leaked into the receiver circuit, causing an unknown and variable power offset in the spectra at the lowest two range gates. Although the spectra shape and velocity information are preserved, the first valid reflectivity estimate is at the third range gate at 0.36 km AGL.

The NOAA S-band VPR (operating at 2.835 GHz) used a stationary dish antenna to form a 2.5° radar beam continuously pointed in the vertical direction (see Fig. 1). The S-band VPR operated in two modes: a precipitation mode and a low-sensitivity mode. Both modes used the same operating parameters listed in Table 1, except during the low-sensitivity mode, a 30-dB attenuator was inserted into the receive signal circuitry to prevent the receiver from saturating at close ranges during intense precipitation (White et al. 2000). Two limitations of the

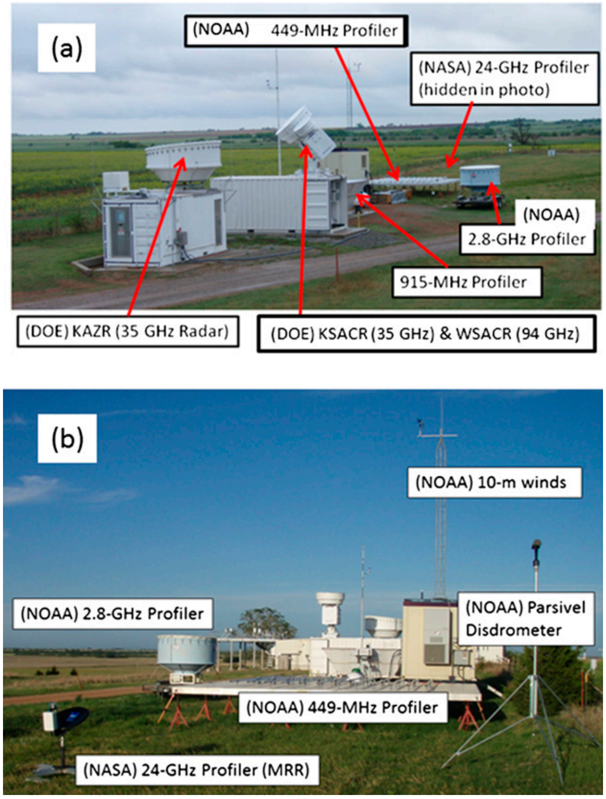

FIG. 1. Radars deployed at the DOE ARM SGP central facility for the MC3E field campaign: (a) view looking west and (b) view looking east.

low-sensitivity mode include the loss of 30-dB sensitivity to detect precipitating clouds above the melting layer in stratiform rain (White et al. 2000) and the increase in reflectivity measurement uncertainty due to a 30-dB decrease in signal-to-noise ratio measurements (Doviak and Zrnić 1993). To overcome these limitations, the S-band VPR was configured to transmit either seven or nine consecutive precipitation mode profiles followed by one low-sensitivity mode profile. During MC3E, only a few precipitation mode profiles contained any sign of saturation in the lowest few range gates. The low-sensitivity mode observations were not used in this study.

The S-band VPR generated a profile of reflectivity-weighted Doppler velocity spectra every 7 s. Three different temporal S-band VPR datasets are available for the community (Williams 2012b): original 7-s dwell, 1-min dwell, and approximately 45-s dwell matched to the 449-MHz VPR temporal resolution (Williams 2012c). For the 1-min and 45-s dwells, the Doppler velocity spectra at each range gate are averaged before estimating the moments of reflectivity, mean radial velocity, and Doppler velocity spectrum width. Both NOAA VPRs were calibrated using a surface two-dimensional video disdrometer (Bartholomew 2011) as discussed in section 3c. NOAA VPR datasets are publically available in the DOE and NASA archives (see www.arm.gov/campaigns/sgp2011midlatcloud and https://gpm.nsstc.nasa.gov/mc3e, respectively).

3. Interpreting Doppler velocity spectra

This section describes the mathematical basis, as well as the methods used to retrieve vertical air motions and DSD parameters from observed 449-MHz and S-band VPR Doppler velocity spectra.

a. *Mathematics of VPR Doppler velocity spectra*

The 449-MHz VPR is sensitive to both Bragg and Rayleigh scattering processes, which result from backscattered energy from changes in refractive index and from hydrometeors, respectively, such that the modeled reflectivity-weighted Doppler velocity spectrum $S_{\mathrm{model}}(v)$ has three terms (Wakasugi et al. 1986),

$$S_{\mathrm{model}}(v) = S_{\mathrm{air}}(v - \overline{v}) + S_{\mathrm{air}}^{\mathrm{norm}}(v - \overline{v}) \otimes S_{\mathrm{hydro}}(v) + \overline{n}, \tag{1}$$

where v is the radar-resolved Doppler velocity (m s^{-1}), $S_{\mathrm{air}}(v - \overline{v})$ is a function describing the air motion (i.e., Bragg scattering signal) with mean radar radial velocity $\overline{v}$, $S_{\mathrm{hydro}}(v)$ is a function describing the hydrometeor motion (i.e., Rayleigh scattering signal) convolved (denoted with the symbol $\otimes$) with the normalized air motion $S_{\mathrm{air}}^{\mathrm{norm}}(v - \overline{v})$, and $\overline{n}$ is the spectrum mean noise level, which is independent of v. Term $\overline{n}$ is estimated for each spectrum as described in Hildebrand and Sekhon (1974) and is not considered a model unknown but is a determined constant for each spectrum. As an example of observed Doppler velocity spectra, Figs. 2a and 2b show profiles of 449-MHz and S-band VPR spectra, respectively, collected at 1205 UTC 20 May 2011. The S-band VPR original 7-s and 62-m vertical range gate spacing spectra have been resampled to match the 449-MHz VPR resolution of 45-s and 106-m vertical spacing. The air motion peak, if observed in the 449-MHz VPR spectra, is always located on the upward side of the Rayleigh scattering peak in the Doppler velocity spectrum, as hydrometeors fall relative to the air motion. Air motion peaks can be observed in the 449-MHz VPR spectra below 2.5 km (Fig. 2a) with retrieved air motion and spectrum width estimates (which are discussed in the next section) shown in all four panels with red vertical tick marks and red horizontal lines, respectively. Note that the air motion peaks are not resolved in the S-band VPR spectra in Fig. 2b. The black dashed lines in Figs. 2a and 2b indicate the 0.66- and 1.66-km heights, which are the heights of the individual 449-MHz and

TABLE 1. Operating parameters for 449-MHz and S-band VPR during MC3E.

Parameter	449-MHz VPR	S-band VPR
Operating frequency	449 MHz	2.8 GHz
Wavelength	66.8 cm	10.4 cm
Peak power	6000 W	380 W
Antenna type	Colinear coaxial array	1.2-m shrouded dish
Beamwidth	9°	2.5°
Interpulse period	120 μs	110 μs
Unambiguous range	18 km	16.5 km
Pulse width	1417 ns	416 ns
Range resolution	212 m	62 m
Range spacing	212 m[a]/106 m[b]	62 m
No. of range gates	77[a]/154[b]	250
Maximum height	16.3 km	15.7 km
Lowest velocity range rate	0.16 km	0.16 km
Lowest reflectivity range gate	0.36 km	0.36 km
No. of coherent integrations	88	15
No. of spectra averaged	16	16
Nyquist velocity	15.7 m s^{-1}	15.8 m s^{-1}
No. of points in spectrum	256	256
Spectral resolution	0.124 m s^{-1}	0.125 m s^{-1}
Dwell time	45 s	7 s
No. of profiles per mode	NA	7 precipitation, 1 low sensitivity[c] 9 precipitation, 1 low sensitivity[d]
Added attenuation	NA	30 dB

[a] Before 9 May.
[b] On and after 9 May.
[c] Before 25 April.
[d] On and after 25 April.

S-band VPR spectra shown in Figs. 2c and 2d, respectively. Two peaks are resolved in the 449-MHz VPR spectra (solid black lines in Figs. 2c and 2d) corresponding to the air motion and hydrometeor motion peaks. In contrast, the S-band VPR spectra (solid cyan lines) detected only the hydrometeor motion peak. The red dashed lines in Figs. 2c and 2d are simulated spectra constructed from the retrieved air motion and DSD parameters and illustrate how well the retrieval technique captures both the Bragg and Rayleigh scattering signals.

The air motion peak can be modeled as a Gaussian-shaped function $S_{\mathrm{air}}(\upsilon-\overline{\upsilon})$ with three parameters describing the backscattered intensity A_{air} (mm^6 m^{-3}), mean radial velocity $\overline{\upsilon}$ (m s^{-1}), and spectrum breadth quantified using the spectrum variance σ^2_{air} (m^2 s^{-2}) (Wakasugi et al. 1987; Gossard 1994),

$$S_{\mathrm{air}}(\upsilon;A_{\mathrm{air}},\overline{\upsilon},\sigma_{\mathrm{air}}) = A_{\mathrm{air}}S^{\mathrm{norm}}_{\mathrm{air}}(\upsilon;\overline{\upsilon},\sigma_{\mathrm{air}}) = A_{\mathrm{air}}\left\{\frac{\exp\left[\dfrac{-(\upsilon-\overline{\upsilon})^2}{2\sigma^2_{\mathrm{air}}}\right]}{\displaystyle\sum_{\upsilon_i=\upsilon_{\min}}^{\upsilon_{\max}}\exp\left[\dfrac{-(\upsilon_i-\overline{\upsilon})^2}{2\sigma^2_{\mathrm{air}}}\right]\Delta\upsilon}\right\} \quad (2)$$

where $\Delta\upsilon$ (m s^{-1}) is the Doppler velocity spectrum resolution, υ_i represents discrete velocities of the spectrum, and the variables $\upsilon_{\min}$ and $\upsilon_{\max}$ are summation limits where $S_{\mathrm{air}}(\upsilon;A_{\mathrm{air}},\overline{\upsilon},\sigma_{\mathrm{air}})$ is above $\overline{n}$. The function $S^{\mathrm{norm}}_{\mathrm{air}}(\upsilon;\overline{\upsilon},\sigma_{\mathrm{air}})$ represents a Gaussian distribution with unity total power return such that

$$\sum_{\upsilon_i=\upsilon_{\min}}^{\upsilon_{\max}} S^{\mathrm{norm}}_{\mathrm{air}}(\upsilon_i;\overline{\upsilon},\sigma_{\mathrm{air}})\Delta\upsilon = 1. \quad (3)$$

The DSD contributes to the hydrometeor motion peak and can be modeled using a normalized Gamma distribution (Testud et al. 2001; Illingworth and Blackman 2002; Bringi et al. 2003) with the raindrop number concentration $N(D)$ [number of drops (mm^{-1} m^{-3})] written as a scaled quasi PDF (Chandrasekar et al. 2005; Seto et al. 2013),

$$N(D;N_w,D_m,\mu) = N_w f(D;D_m,\mu), \quad (4)$$

where

$$f(D;D_m,\mu) = \frac{6}{4^4}\frac{(4+\mu)^{\mu+4}}{\Gamma(\mu+4)}\left(\frac{D}{D_m}\right)^{\mu} \times \exp\left[-(4+\mu)\left(\frac{D}{D_m}\right)\right], \quad (5)$$

N_w [number of drops (mm^{-1} m^{-3})] is the normalized number concentration, μ (unitless) is the gamma-shape

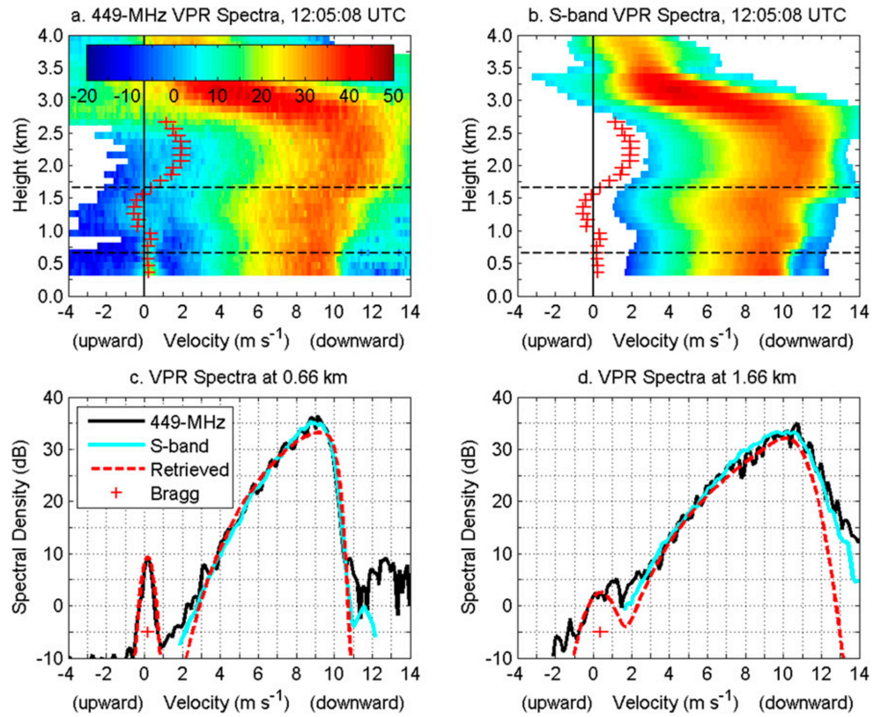

FIG. 2. 449-MHz and S-band VPR reflectivity-weighted Doppler velocity spectra for 45-s dwells starting at 1205:08 UTC 20 May 2011. Profiles of spectra for (a) 449-MHz VPR and (b) S-band VPR. Red vertical marks and horizontal lines indicate mean downward velocity and spectrum breadth, respectively, retrieved from 449-MHz VPR Bragg scattering signal at each range gate. Black solid lines are 449-MHz VPR spectra and cyan solid lines are S-band VPR spectra at (c) 0.66 and (d) 1.66 km. Black dashed lines in (a) and (b) at 0.66 and 1.66 km indicate heights of individual spectra shown in (c) and (d), respectively. Red dashed lines in (c) and (d) are retrieved spectra composed of both Bragg and Rayleigh scattering signals. Colors in (a) and (b) and magnitude in (c) and (d) represent reflectivity spectral density in decibel units calculated using dB $= 10\log[(\mathrm{mm}^6\,\mathrm{m}^{-3})(\mathrm{m\,s}^{-1})^{-1}]$.

parameter, $\Gamma(\ldots)$ is the Euler gamma function, and D_m (mm) is the mass-weighted mean diameter, defined as

$$D_m = \frac{\sum_{D_i=D_{\min}}^{D_{\max}} N(D_i)D_i^4\Delta D}{\sum_{D_i=D_{\min}}^{D_{\max}} N(D_i)D_i^3\Delta D}. \tag{6}$$

The normalized number concentration N_w is defined as

$$N_w = \frac{4^4}{\pi\rho_w}\left(\frac{q}{D_m^4}\right), \tag{7}$$

where ρ_w is density of water ($\rho_w = 1\,\mathrm{g\,cm}^{-3}$ or $\rho_w = 10^{-3}\,\mathrm{g\,mm}^{-3}$) and q ($\mathrm{g\,m}^{-3}$) is the liquid water content, LWC,

$$q = \frac{\pi}{6}\rho_w \sum_{D_i=D_{\min}}^{D_{\max}} N(D_i)D_i^3\Delta D. \tag{8}$$

The normalized number concentration N_w is defined such that given an arbitrary-shaped DSD, N_w is the intercept parameter (the number of raindrops with zero diameter) of an exponential distribution having the same liquid water content q and mean mass-weighted diameter D_m (Testud et al. 2001).

To construct a reflectivity-weighted hydrometeor Doppler velocity spectra $S_{\mathrm{hydro}}(v)$, $N(D)$ is mapped from diameter space into velocity space as described in Atlas et al. (1973) using

$$S_{\mathrm{hydro}}(v; N_w, D_m, \mu) = N(D; N_w, D_m, \mu)D^6\left(\frac{\Delta D}{\Delta v}\right), \tag{9}$$

where D^6 represents raindrop backscattering cross sections assuming Rayleigh scattering, with ΔD and Δv representing the spectra diameter and velocity resolutions, respectively. The mapping from diameter to velocity space depends on the assumed air density–adjusted diameter-to-fall speed relationship, which can be expressed using (Beard 1985)

$$v_f(D;h) = v_f(D;\text{sea level})\left[\frac{\rho_0}{\rho(h)}\right]^{0.45} \tag{10}$$

with a diameter-to-fall speed relationship $v_f(D;h)$ ($\mathrm{m\,s^{-1}}$) of Lhermitte (1990),

$$v_f(D;\text{sea level}) = 9.23[1-\exp(-0.068D^2-0.488D)], \tag{11}$$

where h (m) is the height above sea level, $\rho(h)$ ($\mathrm{kg\,m^{-3}}$) is the air density at h, and ρ_0 ($\mathrm{kg\,m^{-3}}$) is the air density at sea level. The Lhermitte (1990) diameter-to-fall speed relationship is within 1% of the Brandes et al. (2002) fourth-order polynomial relationship and has a smoother asymptotic approach to the maximum surface level $9.23\,\mathrm{m\,s^{-1}}$ fall speed.

Because of turbulent broadening effects within the radar sample volume, which includes vertical air motion, horizontal wind, change of horizontal wind within a range gate (wind shear), and turbulent random motions (Fang et al. 2012), the hydrometeor Doppler velocity spectrum has a broader shape than described in Eq. (9). While these broadening effects depend on the radar beamwidth, the broadening effects do not change the amount of backscattered power detected by the radar. Thus, the broadening effect is modeled by convolving the hydrometeor spectrum $S_{\text{hydro}}(v;N_w,D_m,\mu)$ with the normalized air motion spreading function $S_{\text{air}}^{\text{norm}}(v;\overline{v},\sigma_{\text{air}})$. Also, since the normalized air motion contains $\overline{v}$, the convolution shifts the hydrometeor spectrum by the mean radial velocity, accounting for vertical air motion.

b. Estimating vertical air motion parameters

As shown in Figs. 2c and 2d, the 449-MHz VPR can be sensitive to both Bragg and Rayleigh scattering processes, while the S-band radar is sensitive only to Rayleigh scattering. As the range from the radar increases, the power return from Bragg scattering decreases such that the air motion signal is several orders of magnitude weaker than the hydrometeor motion signal (e.g., see Fig. 2a). Identifying the small-amplitude air motion peak in the same spectrum that contains larger-amplitude hydrometeor motions has been a problem for DSD retrieval algorithms for many years (e.g., Rajopadhyaya et al. 1998; Kanofsky and Chilson 2008). By analyzing spectra from VPRs with different sensitivities to Bragg and Rayleigh scattering, Williams (2012a) developed a technique to subtract the Rayleigh scattering signal observed in one VPR spectra from the spectra that contains both Bragg and Rayleigh scattering signals.

The dual-frequency retrieval technique (Williams 2012) was applied to the 449-MHz and S-band VPR spectra using five main steps. First, the S-band VPR spectra are averaged in time, range, and velocity resolution to match the 449-MHz VPR resolution (as shown in Fig. 2). Second, the S-band VPR spectrum is used to suppress the 449-MHz VPR hydrometeor signal to highlight the small-amplitude Bragg scattering signal. Third, the values of A_{air}, $\overline{v}$, and σ_{air} are estimated assuming a Gaussian-shaped distribution of the form Eq. (2) and minimizing a cost function with spectra expressed in logarithmic units similar to the Rayleigh scattering cost function Eq. (12) discussed in the next section. A height continuity procedure is performed in the penultimate step to interpolate across range gates where Bragg scattering signals were not detected. In the last step, the mean atmospheric air motion $\overline{\varpi}$ is defined to have the same magnitude as $\overline{v}$ but is defined so that upward motion is positive.

c. Estimating DSD parameters

Since both the 449-MHz and S-band VPRs observe Rayleigh scattering from hydrometeors, spectra from either VPR can be used to estimate DSD parameters as long as the turbulent spectrum broadening effects are estimated for the different VPR radar beamwidths. To avoid estimating S-band VPR broadening effects from the retrieved 449-MHz VPR turbulent broadening term σ_{air}, the DSD parameters were estimated using the hydrometeor motion peak in the 449-MHz VPR spectra. The 449-MHz VPR hydrometeor motion is modeled with six unknowns: three associated with air motion ($A_{\text{air}}, \overline{v}$, and σ_{air}) and three associated with the DSD (N_w, D_m, and μ). To reduce the complexity of the retrieval procedure, the three air motion parameters (described in section 3b) are estimated first and then held constant while estimating the three DSD parameters.

The retrieval method uses a forward-modeling technique simulating Doppler velocity spectra for all possible (D_m, μ) pairs with D_m ranging from 0.3 to 4.0 mm in 0.01 increments and μ ranging from -0.9 to 21 in 0.1 increments (Williams and Gage 2009). For each possible (D_m, μ) pair, N_w is estimated from the observed reflectivity using Eqs. (5) and (13), which is discussed in the next section. For each possible (N_w, D_m, and μ) triplet, a model spectrum $S_{\text{model}}(v)$ is produced using Eq. (1) with constant $\overline{v}$ and spectrum-broadening σ_{air} and then compared with $S_{\text{obs}}(v)$ using a cost function,

$$\gamma^2 = \sum_{v_i=v_{\min}}^{v_{\max}} \{10\log[S_{\text{obs}}(v_i)] - 10\log[S_{\text{model}}(v_i)]\}^2, \tag{12}$$

where $v_{\min}$ and $v_{\max}$ define the range of velocities with $S_{\text{obs}}(v_i)$ above $\overline{n}$. The model spectrum with the lowest

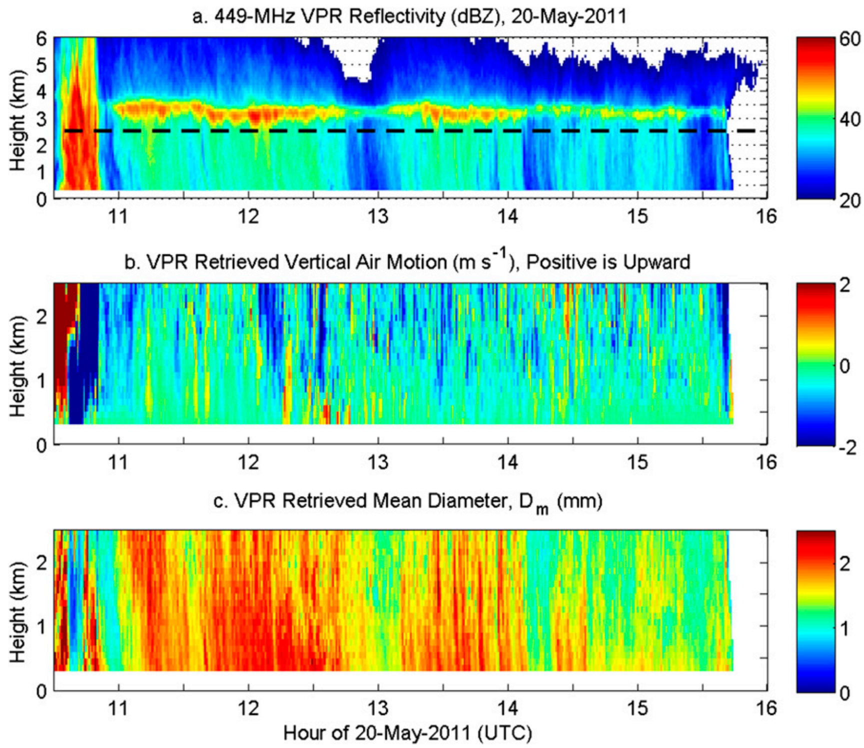

FIG. 3. Time–height cross sections of (a) observed 449-MHz VPR reflectivity (dBZ) from 0.36 to 6 km, (b) retrieved vertical air motion (m s^{-1}), and (c) retrieved mass-weighted mean diameter (mm) from 0.36 to 2.5 km. Black dashed line at 2.5 km in (a) is a visual guide indicating maximum height of retrievals shown in (b) and (c). Upward air motions are in shades of red and downward air motions are in shades of blue.

cost function is selected independent of neighboring time–height solutions. Also, retrievals were performed at the 45-s 449-MHz VPR temporal resolution with DSD parameters resampled to 1-min resolution for calibration and disdrometer comparisons.

The 20 May 2011 rain event passing over the SGP central facility consisted of stratiform rain with well-defined radar bright bands and deep convective rain with reflectivity exceeding 50 dBZ below 3 km as illustrated in the 449-MHz VPR reflectivity in Fig. 3a. Figure 3b shows the vertical structure of dual-frequency-retrieved air motion $\overline{\omega}$, and Fig. 3c shows the retrieved D_m. The dashed line in Fig. 3a indicates the 2.5-km height, which is the maximum height of detected air motion and DSD retrievals shown in Figs. 3b and 3c, respectively. Even though the reflectivity structure contains radar brightband signatures, the vertical air motions exceed 2 m s^{-1} downdrafts (blue colors) and 2 m s^{-1} updrafts (red colors) underneath the radar bright band, indicating embedded convection within stratiform rain.

The 449-MHz and S-band VPRs were calibrated by comparing VPR reflectivity at 0.36 km with reflectivities from a surface 2D video disdrometer (2DVD) for the stratiform rain from 1140 through 1530 UTC, which are shown in Fig. 4a. Note that 2DVD disdrometer data are not available prior to 1140 UTC. The VPR calibrations were adjusted until the mean reflectivity difference (profiler minus 2DVD) was zero with Fig. 4c showing the scatterplot of reflectivity differences versus 449-MHz VPR reflectivities. The Pearson correlation coefficient between VPR reflectivities was $r_{449\mathrm{MHz\text{-}Sband}} = 0.986$ and between the 449-MHz VPR and 2DVD was $r_{449\mathrm{MHz\text{-}2DVD}} = 0.924$. The reflectivity difference standard deviations were 0.68 and 1.42 dBZ between the two VPRs and between (449-MHz VPR minus 2DVD) observations, respectively. The larger reflectivity spread between the VPR and disdrometer is probably due to different instrument-measuring techniques (i.e., volume backscattered energy vs drop counting) and due to different instrument sample volumes. Figure 4b shows the time series of D_m retrieved from the profiler observations at 0.36 km and estimated from the surface 2DVD disdrometer with a Pearson correlation coefficient of $r_{\mathrm{VPR\text{-}2DVD}} = 0.890$. A scatterplot of

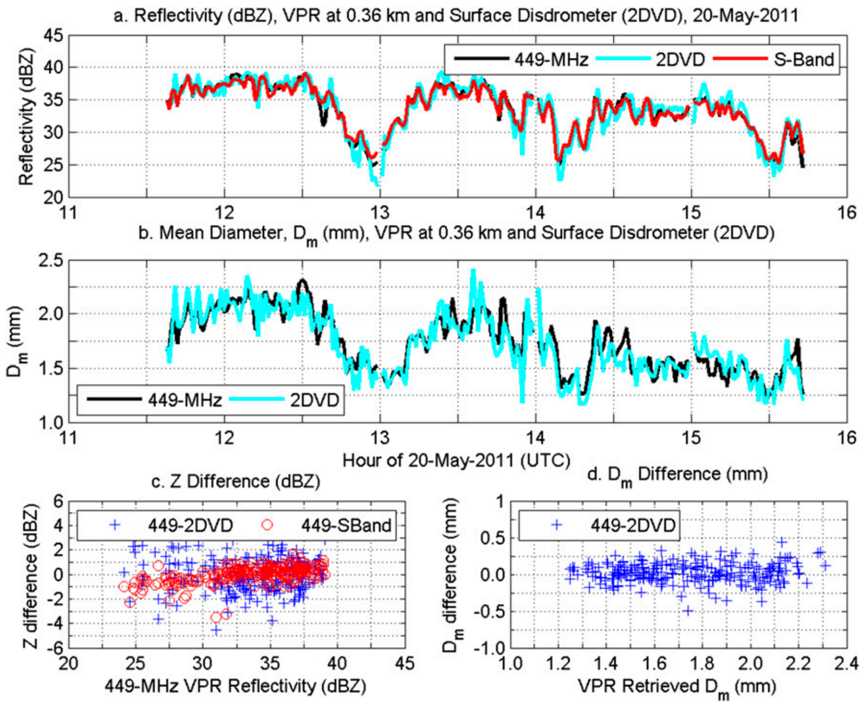

FIG. 4. Calibration of 449-MHz and S-band VPR using surface disdrometer observations during stratiform rain event from 1100 to 1600 UTC 20 May 2011: (a) 449-MHz (black) and S-band (red) VPR reflectivity (dBZ) at 0.36 km, and surface 2DVD disdrometer reflectivity (cyan). Pearson correlation coefficients were $r_{\text{449MHz-2DVD}} = 0.924$ and $r_{\text{449MHz-Sband}} = 0.986$. (b) Mass-weighted mean diameter (mm) retrieved by VPRs at 0.36 km and estimated from surface 2DVD disdrometers, and the Pearson correlation coefficient for this time interval was $r_{\text{VPR-2DVD}} = 0.890$. (c) Scatterplot of reflectivity differences (449-MHz VPR minus 2DVD) (blue plusses) with a standard deviation of 1.42 dBZ and (449-MHz VPR minus S-band VPR) (red circles) with a standard deviation of 0.68 dBZ. (d) Scatterplot of mean diameter differences (VPR minus 2DVD) with bias and a standard deviation of 0.02 and 0.13 mm, respectively.

D_m differences (profiler minus 2DVD) shown in Fig. 4d have a mean difference (bias) and a standard deviation of 0.02 and 0.13 mm, respectively.

4. Decomposing reflectivity

Although Figs. 3a and 3c show the vertical structure of reflectivity and D_m, it is difficult to determine how much of the reflectivity variations are due to variations in D_m because reflectivity and D_m are measured in different units (dBZ vs mm). Since the DSD is described as a quasi PDF in Eq. (4), reflectivity can be decomposed into two terms associated with DSD intensity using N_w and DSD shape using $f(D; D_m, \mu)$, which is defined in Eq. (5). The DSD reflectivity in linear units (mm^{-6} m^{-3}) can be expressed as

$$z = N_w \sum_{D_i = D_{\min}}^{D_{\max}} f(D_i; D_m, \mu) D_i^6 \Delta D \tag{13}$$

and in logarithmic units (dBZ) as

$$Z = 10\log(N_w) + 10\log\left[\sum_{D_i = D_{\min}}^{D_{\max}} f(D_i; D_m, \mu) D_i^6 \Delta D\right]. \tag{14}$$

The first term on the right-hand side in Eq. (14) is only a function of N_w. The second term on the right-hand side is a function of the DSD shape determined by D_m and μ. To simplify notation, Eq. (14) is rewritten as

$$Z = N_w^{\text{dB}} + I_b^{\text{dB}}(D_m, \mu), \tag{15}$$

where

$$N_w^{\text{dB}} = 10\log(N_w) \tag{16}$$

and

$$\begin{aligned} I_b^{\text{dB}}(D_m, \mu) &= 10\log[F(D_m, \mu)] \\ &= 10\log\left[\sum_{D_i = D_{\min}}^{D_{\max}} f(D; D_m, \mu) D^6 \Delta D\right] \end{aligned} \tag{17}$$

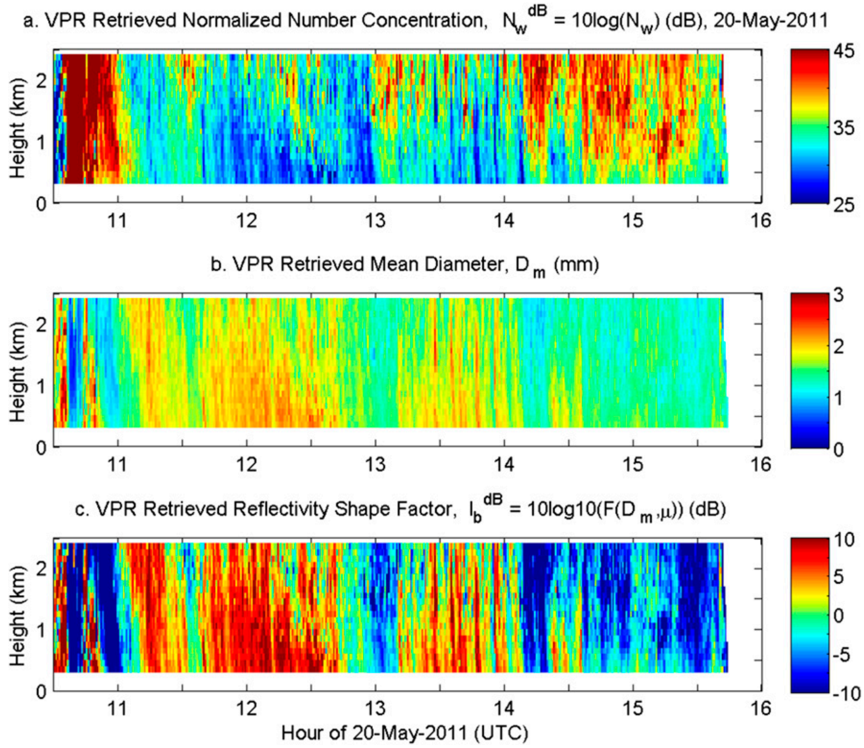

FIG. 5. Time–height cross sections during the 20 May 2011 rain event of (a) VPR retrieved normalized number concentration expressed in logarithmic units $N_w^{\mathrm{dB}} = 10\log(N_w)$ (dB), (b) VPR retrieved mean mass-weighted raindrop diameter D_m (mm), and (c) VPR retrieved reflectivity shape factor in logarithmic units $I_b^{\mathrm{dB}} = 10\log[F(D_m, \mu)]$ (dB).

are in logarithmic units (dB) and I_b^{dB} is the reflectivity shape factor and is equivalent to the normalized backscattering reflectivity, which is the reflectivity with $N_w = 1$ (Meneghini et al. 2003).

Figure 5 shows the reflectivity (see Fig. 3a) decomposed into N_w^{dB} (Fig. 5a), D_m (Fig. 5b), and I_b^{dB} (Fig. 5c) for the convective core and stratiform rain period from 1030 to 1600 UTC during the 20 May 2011 rain event. During the stratiform rain (from approximately 1100 to 1530 UTC), both D_m and I_b^{dB}, in general, increase in magnitude as the raindrops fall through the atmosphere. Interestingly, N_w^{dB} and I_b^{dB} (Figs. 5a and 5c, respectively) have compensating vertical structures with N_w^{dB} decreasing as I_b^{dB} increases.

Through Eq. (15), reflectivity, N_w^{dB}, and I_b^{dB} are related such that an increase or decrease in one quantity must be compensated by one or both of the other quantities. Figure 6 illustrates a reflectivity vertical decomposition diagram (Z-VDD) that decomposes reflectivity into N_w^{dB} and I_b^{dB} vertical structures during a 10-min window starting at 1200 UTC. The top three panels show the vertical structure of reflectivity (Fig. 6a), N_w^{dB} (Fig. 6b), and I_b^{dB} (Fig. 6c) with each symbol representing an individual 45-s observation or retrieval with symbol color representing the height of the specific range gate. A 10-min window allows for the characterization of precipitation vertical structures over an averaged 10-min by 3-km time–space domain (assuming $5\,\mathrm{m\,s^{-1}}$ advection speed during the 10-min interval) to avoid characterizing instantaneous vertical structures dominated by advecting precipitation fall streaks (i.e., several short-duration reflectivity fall streaks appear in Fig. 3a). The black line in each panel is the mean value at each range gate. From Figs. 6a–c, we can see that reflectivity is nearly constant with height, while N_w^{dB} decreases and I_b^{dB} increases with decreasing height. To see the relative contributions of N_w^{dB} and I_b^{dB} to reflectivity, Fig. 6d shows a scatterplot of N_w^{dB} versus I_b^{dB} using the same color scheme used in Figs. 6a–c, so that red symbols are from 2.5-km height and blue symbols are from 0.36-km height. The diagonal lines in Fig. 6d represent constant reflectivities with the same color code and line patterns used in Fig. 6a. For this 10-min window, Fig. 6d illustrates that reflectivity was nearly constant as N_w^{dB} decreased and I_b^{dB} increased with decreasing height. This compensating pattern indicates raindrop *evolution* with height, while reflectivity remains relatively constant. Since all quantities are in logarithmic units, changes of 1,

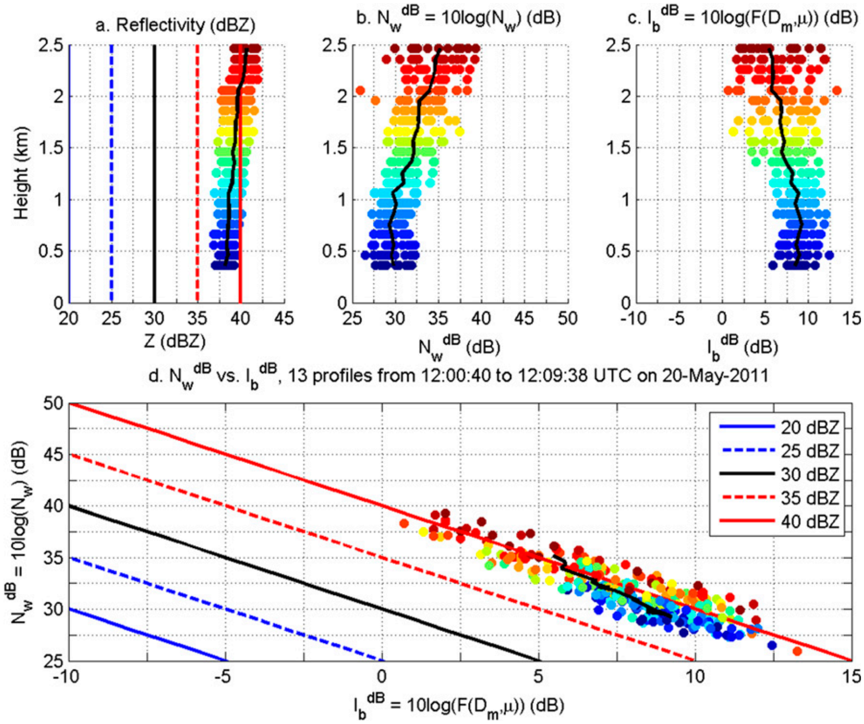

FIG. 6. Reflectivity vertical decomposition diagram (Z-VDD) for 13 profiles during the 10-min interval starting at 1200 UTC 20 May 2011. (a)–(c) The reflectivity (dBZ), normalized number concentration $N_w^{\rm dB} = 10\log(N_w)$ (dB), and reflectivity shape factor $I_b^{\rm dB} = 10\log[F(D_m, \mu)]$ (dB) as a function of height, respectively. The reflectivity shown in (a) is the summation of $N_w^{\rm dB}$ and $I_b^{\rm dB}$ shown in (b) and (c) as discussed near Eq. (15). Symbol color represents height. (d) Scatterplot of $N_w^{\rm dB}$ vs $I_b^{\rm dB}$ with symbol colors representing heights shown in (a)–(c). Diagonal lines in (d) represent constant reflectivity using the same color and line patterns used in (a). Mean values at each range gate in (a)–(c) are shown with solid black lines in each panel.

2, and 3 dB represent relative change of 26%, 58%, and 100%, respectively. As discussed in the next section, expressing the DSD parameters in the liquid water content domain provides better insight into evaporation, breakup, and coalescence processes than expressing DSD parameters in the reflectivity domain.

To examine multiple profiles of observations on the same graph, the reflectivity vertical evolution can be shown using scatterplots similar to Fig. 6d but using 10-min mean profiles to represent the vertical evolution. Figure 7a shows a scatterplot of $N_w^{\rm dB}$ versus D_m for each 10-min mean profile with the color of symbols representing the profile time from 1030 to 1530 UTC. The black diagonal line is a convective–stratiform separation line following the derivation in Thurai et al. (2010) expressed as $N_w^{\rm separation} = 10\log(-1.65D_m + 6.36)$. Observations from 1030 to 1100 UTC are above this separation line, which was during the passage of the convective core. After 1100 UTC, the 10-min profiles approach the convective–stratiform separation line and do not fall below the separation line until after 1300 UTC, indicating that the separation line is an approximate convective–stratiform regime indicator. Figure 7b shows a scatterplot of $N_w^{\rm dB}$ versus $I_b^{\rm dB}$ for each 10-min mean profile. The diagonal lines represent constant reflectivity. It is interesting to note that the stratiform profiles suggest a positive relationship between reflectivity and $I_b^{\rm dB}$. Since $I_b^{\rm dB}$ is not dependent on N_w, such a relationship could be used to constrain the DSD shapes in underconstrained satellite retrieval algorithms (Williams et al. 2014). This will be a topic for future research.

5. Decomposing liquid water content

The previous section decomposed reflectivity into $N_w^{\rm dB}$ and $I_b^{\rm dB}$ to study the evolution of raindrops within the reflectivity domain. But if the decomposition were performed in the LWC domain, then changes in height could be directly related to evaporation or accretion processes and to net breakup or net coalescence processes occurring in the vertical column. Also, since N_w is a normalized parameter with unusual physical interpretation, Tapiador et al. (2014) suggest scaling DSD distributions with the total number of drops per unit

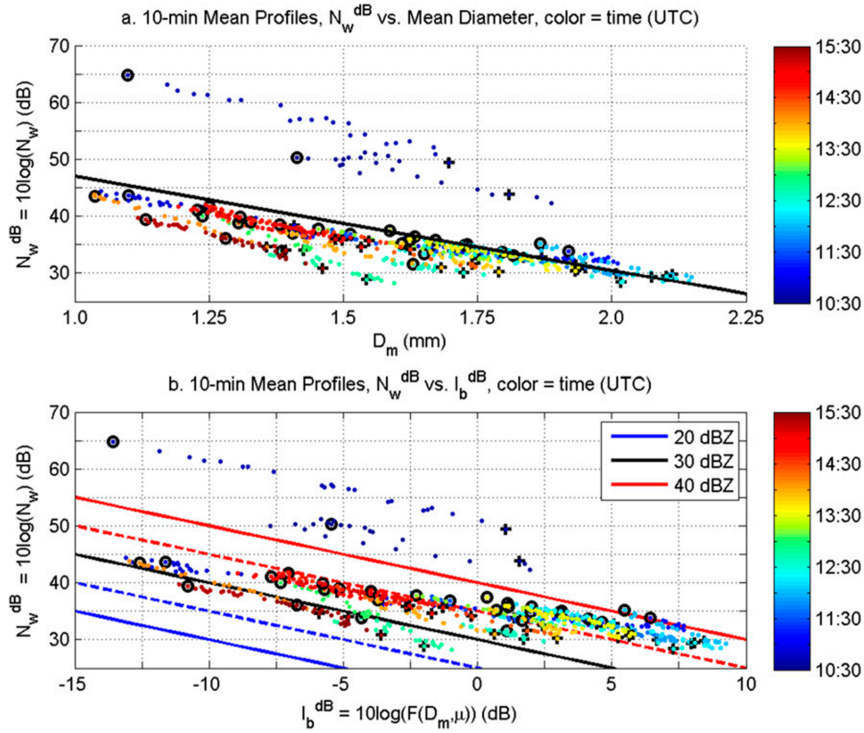

FIG. 7. Scatterplot of $N_w^{\mathrm{dB}} = 10\log(N_w)$ (dB) vs (a) D_m (mm) and (b) $I_b^{\mathrm{dB}} = 10\log[F(D_m, \mu)]$ (dB) for each 10-min mean profile from 1030 to 1530 UTC 20 May 2011. Colors represent the time of the profile with dark blue indicating 1030 UTC and dark red indicating 1530 UTC. Circle symbol represents the maximum height (2.5 km) of the profile, and plus symbol represents the lowest height (0.36 km) of the profile. Black diagonal line in (a) represents a convective–stratiform transition line following Thurai et al. (2010) using $N_w^{\mathrm{separation}} = 10\log(-1.65D_m + 6.36)$ (dB) with observations above the line classified as convective rain and observations below the line classified as stratiform rain. Diagonal lines in (b) represent constant reflectivity using the same color and line type used in Figs. 6a and 6d.

volume N_t (m^{-3}) so that the number concentration is a scaled PDF described using

$$N(D; N_t, D_m, \mu) = N_t g(D; D_m, \mu), \qquad (18)$$

where

$$g(D; D_m, \mu) = \frac{(4+\mu)^{\mu+1}}{\Gamma(\mu+1)D_m}\left(\frac{D}{D_m}\right)^{\mu} \times \exp\left[-(4+\mu)\left(\frac{D}{D_m}\right)\right]. \qquad (19)$$

Using Eq. (8), the liquid water content can be expressed in linear units (g m^{-3}) as

$$q = N_t \frac{\pi}{6}\rho_w \sum_{D_i=D_{\min}}^{D_{\max}} g(D_i; D_m, \mu) D_i^3 \Delta D \qquad (20)$$

and in logarithmic units (dB) as

$$q^{\mathrm{dB}} = N_t^{\mathrm{dB}} + D_q^{\mathrm{dB}}, \qquad (21)$$

where

$$q^{\mathrm{dB}} = 10\log(q), \qquad (22)$$

$$N_t^{\mathrm{dB}} = 10\log(N_t), \qquad (23)$$

and the LWC shape factor is

$$D_q^{\mathrm{dB}} = 10\log[G(D_m, \mu)] = 10\log\left[\frac{\pi}{6}\rho_w \sum_{D_i=D_{\min}}^{D_{\max}} g(D_i; D_m, \mu) D_i^3 \Delta D\right]. \qquad (24)$$

While it is possible to calculate N_t directly using VPR spectra, it is easier to estimate N_t from retrieved values of (N_w, D_m, μ) by rearranging Eqs. (4), (5), and (18) to yield

$$N_t = N_w \frac{6(4+\mu)^3}{4^4(\mu+3)(\mu+2)(\mu+1)} D_m. \qquad (25)$$

The simplest physical interpretation of Eq. (21) is that the total liquid water content is controlled, or dependent

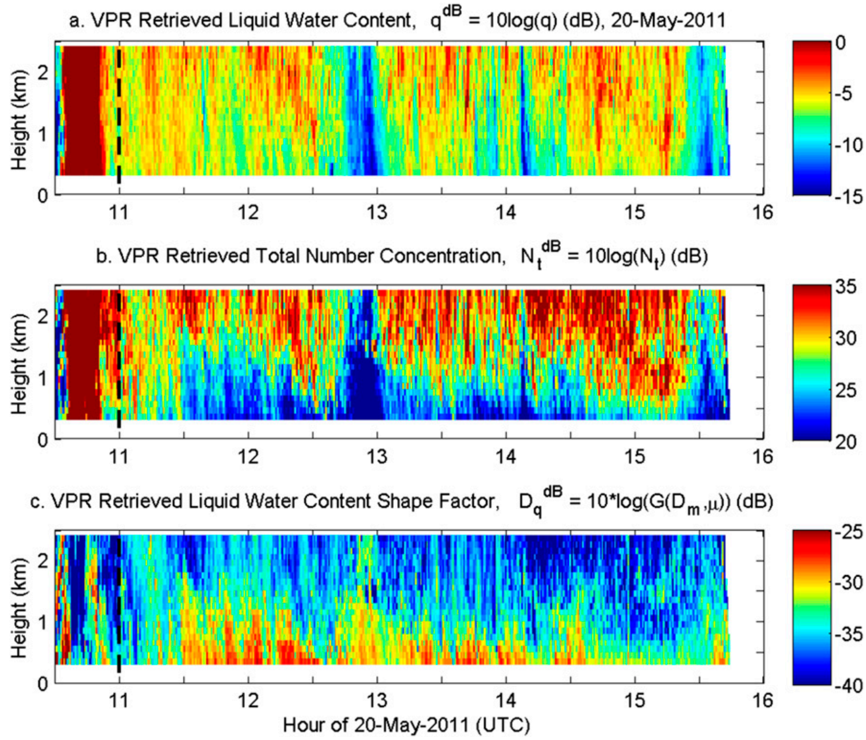

FIG. 8. Time–height cross sections during the 20 May 2011 rain event of (a) $q^{\mathrm{dB}} = 10\log(q)$ (dB), (b) $N_t^{\mathrm{dB}} = 10\log(N_t)$ (dB), and (c) $D_q^{\mathrm{dB}} = 10\log[G(D_m, \mu)]$ (dB). To aid visualizing changes between panels, the color scales in (b)–(d) each span 15 units.

on, the total number of raindrops per unit volume and the DSD mean size and breadth. This follows the logic of ‘‘number control’’ or ‘‘size control’ microphysical processes as postulated by Steiner et al. (2004). When q^{dB} is constant with height, then changes in total number of drops per unit volume N_t^{dB} will be compensated with opposite changes in LWC shape factor D_q^{dB}.

Figure 8 shows the vertical structure of retrieved liquid water content q^{dB} (Fig. 8a), total number concentration N_t^{dB} (Fig. 8b), and LWC shape factor D_q^{dB} (Fig. 8c) from 1030 to 1600 UTC 20 May 2011. The updraft/downdraft couplet shown in Fig. 3b during the passage of the convective cell illustrates how dynamics complicates an analysis of breakup and coalescence processes within convective cells. Since only a few convective cell profiles were sampled during the 20 May 2011 event, the LWC vertical structure was analyzed only during the stratiform rain after 1100 UTC, which is indicated with vertical black dashed lines in Fig. 8. The radar reflectivity bright band in Fig. 3a provides stratiform regime context for the LWC parameters shown in Fig. 8. In general, while q^{dB} tends to decrease as the raindrops fall below 2.5 km, N_t^{dB} decreases more and is compensated with increasing D_q^{dB}.

To investigate the LWC vertical structure, Fig. 9 shows the LWC-VDD using the same format as the Z-VDD shown in Fig. 6 and for the same 10-min interval starting at 1200 UTC 20 May 2011. The top three panels show the vertical structure of q^{dB} (Fig. 9a), N_t^{dB} (Fig. 9b) and D_q^{dB} (Fig. 9c). The black line in each panel is the mean value at each range gate. Figure 9d shows a scatterplot of N_t^{dB} versus D_q^{dB} using the same color scheme used in Figs. 9a–c to show the height evolution on the N_t^{dB}–D_q^{dB} domain. The diagonal lines represent constant q^{dB} values with the same color code used in Fig. 9a. Perpendicular deviations from the parallel constant q^{dB} lines indicate net evaporation or accretion.

For this profile the mean q^{dB} (Fig. 9a) decreases by approximately 3 dB, representing a 50% loss in mass over this 2-km altitude, suggesting net evaporation for this profile. An examination of N_t^{dB} and D_q^{dB} reveals that N_t^{dB} is decreasing and that D_q^{dB} is increasing with decreasing altitude. A 9-dB decrease of N_t^{dB} represents almost an order of magnitude decrease in the number of drops per unit volume, suggesting a combination of net evaporation (since q^{dB} decreases) and net coalescence of raindrops over this 2-km altitude. Since q^{dB} and N_t^{dB} decreased by approximately 3 and 9 dB, respectively, D_q^{dB} compensates these decreases with an increase of approximately 6 dB.

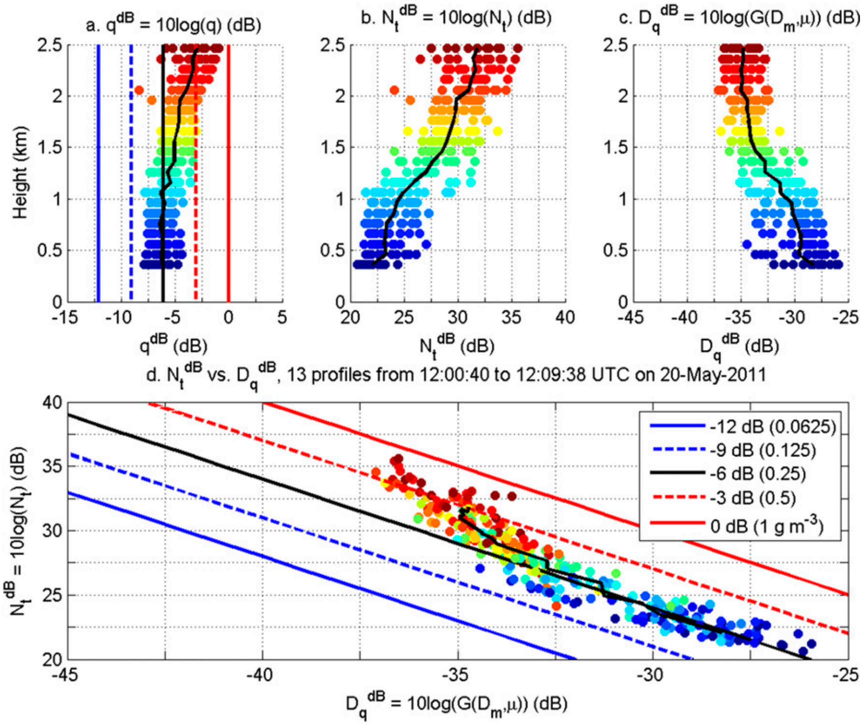

FIG. 9. As in Fig. 6, except for quantities in the LWC domain to generate a LWC-VDD for 13 profiles during the 10-min interval starting at 1200 UTC 20 May 2011: (a) $q^{\mathrm{dB}} = 10\log(q)$ (dB), (b) $N_t^{\mathrm{dB}} = 10\log(N_t)$ (dB), and (c) $D_q^{\mathrm{dB}} = 10\log[G(D_m, \mu)]$ (dB). The q^{dB} shown in (a) is the summation of N_t^{dB} and D_q^{dB} shown in (b) and (c), respectively, as discussed near Eq. (21). (d) Scatterplot of N_t^{dB} vs D_q^{dB} with symbol colors representing heights shown in (a)–(c). Diagonal lines represent constant LWC in logarithmic units [linear units (g m^{-1}) shown in parentheses] using the same color and line patterns used in (a). Mean values at each range gate in (a)–(c) are shown with solid black lines in each panel.

To evaluate multiple LWC profiles during this stratiform rain event, a scatterplot similar to Fig. 9d is constructed in Fig. 10 using the 10-min mean profiles of N_t^{dB} and D_q^{dB}. The colors indicate the profile time from 1100 to 1530 UTC, and the constant q^{dB} lines are spaced 3 dB apart to identify net evaporation or accretion. The circle symbol represents the maximum profile height of 2.5 km. This scatterplot shows a general trend of decreasing q^{dB} with decreasing altitude, suggestive of net evaporation in the 10-min mean profiles.

From Fig. 10, we can deduce that microphysical processes are identified with changes in q^{dB}, N_t^{dB}, and D_q^{dB} with altitude; thus, these altitude-dependent changes are the microphysical ‘‘fingerprints’’ derived from radar observations (Kumjian and Prat 2014). To objectively determine how much a variable changes over 2-km altitude, a line of the form $y = mx + b$ was determined for each 10-min mean profile. Then, the change between 2.5 and 0.36 km was determined for each profile. Figure 11 shows the vertical evolution diagram (VED) in both reflectivity and LWC domains. In the reflectivity domain (Fig. 11a), ΔN_w^{dB} is plotted versus ΔI_b^{dB} with the symbol color representing reflectivity. The diagonal line represents profiles having a constant reflectivity with height. Estimates plotted below the diagonal line come from profiles having decreasing reflectivity with decreasing height. In most 10-min average profiles, reflectivity is decreasing with height so that symbols are plotted below the diagonal line. Also, ΔN_w^{dB} tends to decrease and ΔI_b^{dB} tends to increase as the raindrops fall so that ΔN_w^{dB} is negative and ΔI_b^{dB} is positive in most of the 10-min average profiles.

The LWC vertical evolution diagram (LWC-VED) (Fig. 11b) provides more insight into the microphysical processes with ΔN_t^{dB} plotted versus ΔD_q^{dB} and the symbol color representing q^{dB}. Since ΔN_t^{dB} was negative and ΔD_q^{dB} was positive in all 10-min mean profiles, only one quadrant of possible solutions is shown in Fig. 11b, suggesting that net coalescence was dominant as the DSD evolved with height. The diagonal black solid line represents profiles having a constant LWC with height. The black dashed line represents profiles that lose 50%

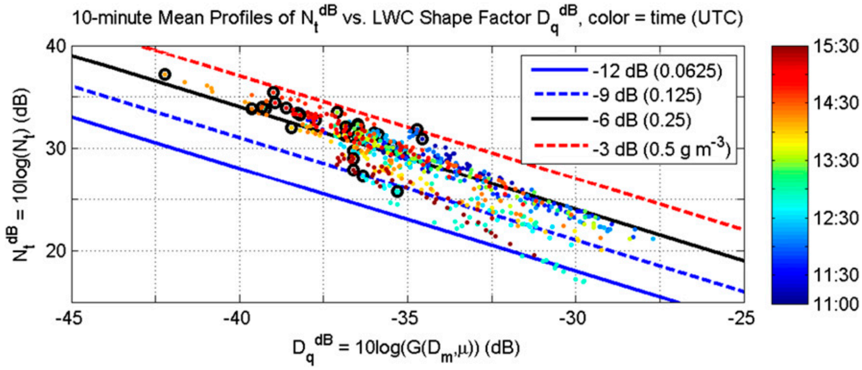

FIG. 10. As in Fig. 7b, except for $N_t^{\mathrm{dB}} = 10\log(N_t)$ vs $D_q^{\mathrm{dB}} = 10\log[G(D_m, \mu)]$ for each 10-min mean profile from 1100 to 1530 UTC 20 May 2011. Colors represent the time of the profile with dark blue indicating 1100 UTC and dark red indicating 1530 UTC. Diagonal lines represent q^{dB} using the same color and line types used in Figs. 9a and 9d.

of their mass through net evaporation over the 2-km fall distance corresponding to $\Delta q^{\mathrm{dB}} = -3\,\mathrm{dB}$. All 10-min profiles showed either a nearly constant or a decrease in LWC over the 2-km altitude, suggesting that net evaporation was either neutral or positive during this stratiform rain event.

6. Conclusions

The Midlatitude Continental Convective Clouds Experiment (MC3E) was a 2-month field campaign centered in northern Oklahoma with a goal of observing the dynamical and microphysical properties of precipitating

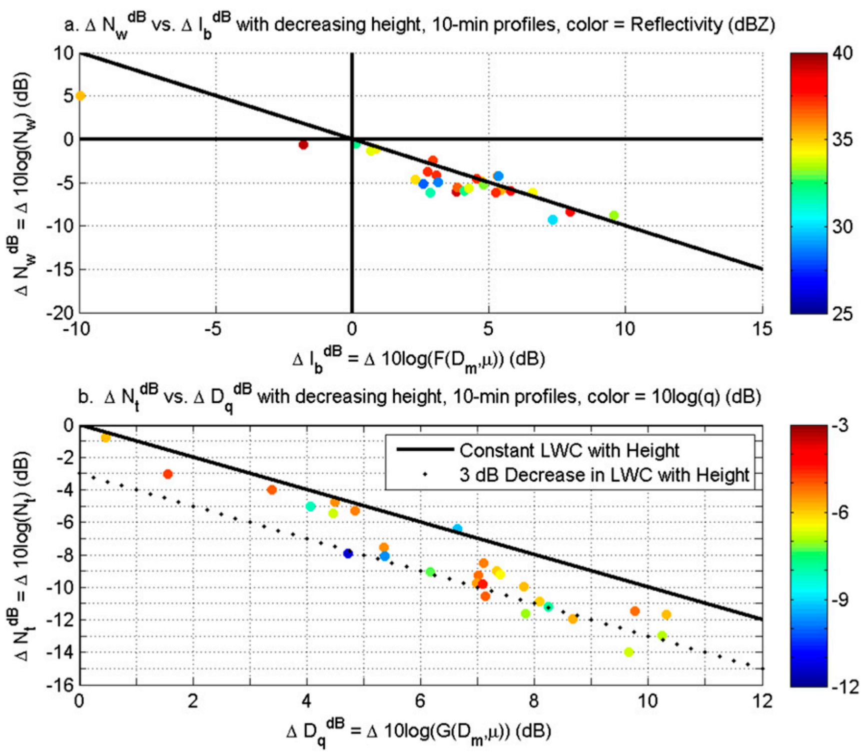

FIG. 11. Vertical evolution diagrams for retrievals expressed in (a) reflectivity domain using (N_w^{dB}, I_b^{dB}) and in (b) LWC domain using (N_t^{dB}, D_q^{dB}). Each symbol represents change in intensity (either ΔN_w^{dB} or ΔN_t^{dB}) vs change in shape factor (either ΔI_b^{dB} or ΔD_q^{dB}) over the 2-km height range from 2.5 to 0.36 km. Symbol color represents profile (a) mean reflectivity (dBZ) or (b) mean $q^{\mathrm{dB}} = 10\log(q)$ (dB). Solid diagonal line represents constant (a) reflectivity or (b) LWC over the 2-km height range. Dashed diagonal line in (b) represents a decrease of $\Delta q^{\mathrm{dB}} = -3\,\mathrm{dB}$ over the 2 km, indicating net evaporation with 50% loss of mass in the vertical profile.

convective cloud systems in the central Plains. Using reflectivity-weighted Doppler velocity spectra recorded by two vertically pointing radars (VPRs) operating side by side and at 449 MHz and 2.835 GHz (S band) enabled vertical air motion and raindrop size distribution (DSD) parameters to be retrieved from near the surface to just below the melting layer approximately 2.5 km above the ground. The retrieval technique employed in this work utilized the 449-MHz VPR sensitivity to both turbulent air motion and raindrop motion along with the S-band VPR's sensitivity to raindrop motion to isolate and then retrieve vertical air motion during precipitation. After estimating the vertical air motion, the DSD parameters were retrieved by fitting a gamma-shaped DSD model to the raindrop motion portion in the calibrated reflectivity-weighted Doppler velocity spectra. The retrieved DSD parameters were the normalized number concentration N_w, mean raindrop diameter D_m, and shape parameter μ, which are publically available on the DOE and NASA field campaign archives (www.arm.gov/campaigns/sgp2011midlatcloud and https://gpm.nsstc.nasa.gov/mc3e, respectively).

The DSD vertical structure was investigated in both the reflectivity and liquid water content (LWC) domains. Within the reflectivity domain, it was difficult to associate changes in reflectivity with changes in N_w or D_m because all three parameters have different units (i.e., dBZ, mm^{-1} m^{-3}, and mm). To overcome this difficulty, reflectivity was decomposed into two logarithmic terms with one term associated with number concentration $N_w^{\mathrm{dB}} = 10\log(N_w)$ and another term associated with DSD shape I_b^{dB}. With all terms in logarithmic units, a change of 1, 2, or 3 dB corresponds to a relative change of 26%, 58%, or 100%, respectively. The reflectivity vertical decomposition diagram (Z-VDD) was introduced and allows for investigation of interactions between Z, N_w^{dB}, and I_b^{dB} in the vertical column. During stratiform rain on 20 May 2011, reflectivity changed only by a couple decibels (dBZ) in the vertical column, while N_w^{dB} tended to decrease and I_b^{dB} tended to increase as the raindrops fell below the radar bright band. This compensating pattern in N_w^{dB} and I_b^{dB} is consistent with net raindrop coalescence because the raindrop number concentration decreased and the mean raindrop size increased as the raindrops fell.

Understanding that analysis of DSD vertical structure within the reflectivity domain does not provide a direct estimate of evaporation; the DSD vertical structure was studied within the LWC domain. Since N_w is a normalized quantity representing the intercept value of an exponential-shaped DSD given an arbitrary-shaped DSD with LWC and D_m, it is difficult to interpret the physical meaning of N_w^{dB} as it changes with height. To overcome this challenge, the retrieved N_w parameter was converted to the physical quantity of total number concentration N_t (i.e., the total number of raindrops per unit volume). In this transformation, D_m and μ were unchanged.

To investigate raindrop evaporation and net raindrop breakup and coalescence, LWC was decomposed into three logarithmic terms: one term representing LWC, $q^{\mathrm{dB}} = 10\log(q)$; one term representing the total number concentration, $N_t^{\mathrm{dB}} = 10\log(N_t)$; and another representing the mass distribution shape, D_q^{dB}. During stratiform rain on 20 May 2011, the newly introduced LWC vertical decomposition diagram (LWC-VDD) showed a compensating pattern with N_t^{dB} decreasing and D_q^{dB} increasing as the raindrops fell. This pattern is consistent with net coalescence. In addition to this coalescence signature, the LWC-VDD also showed that LWC decreased as the raindrops fell a distance of 2 km under a well-defined radar bright band consistent with net evaporation in the vertical column. The usefulness of expressing LWC in logarithm units is that it allows for direct estimation of net evaporation (or accretion) with a change of -3 dB, indicating a 50% loss of mass.

Though radar observations and DSD retrievals provide snapshots of microphysical states at discrete times and heights, the vertical change of q^{dB}, N_t^{dB}, and D_q^{dB} with height provide insights into microphysical processes occurring vertically. The LWC vertical evolution diagram (LWC-VED) showed changes in Δq^{dB}, ΔN_t^{dB}, and ΔD_q^{dB} over a 2-km fall distance, allowing the evaporation and breakup or coalescence processes from multiple profiles to be plotted on the same graph. In the stratiform rain event studied, LWC-VEDs of 10-min profiles showed that evaporation ranged from neutral to approximately 50% loss of mass and that net coalescence dominated as ΔN_t^{dB} was negative and ΔD_q^{dB} was positive as the raindrops fell over a 2-km distance.

In closing, this study introduced Z-VDD and LWC-VDD as graphical tools to analyze raindrop net evaporation and net raindrop breakup or coalescence in the vertical column. Since the LWC-VDD is not limited to radar observations, the LWC-VDD will be used in the future as a tool to evaluate net evaporation and net breakup or coalescence in numerical models. Numerical models using a two-moment microphysical scheme generate N_t and a mixing ratio (mass of water normalized by mass of air within a unit volume) (Morrison et al. 2012) that can be directly mapped into the LWC-VDD after estimating D_q^{dB} using Eqs. (21)–(24). Thus, the LWC-VDD will be a technique to bridge radar observations and numerical model outputs in order to help understand observed and modeled microphysical processes in terms of number-controlled and size-controlled processes as discussed in Steiner et al. (2004).

Acknowledgments. Support for this work was provided by Ramesh Kakar under the NASA Precipitation Measurement Mission (PMM) and NASA Global Precipitation Measurement (GPM) mission Grant NNX13AF86G and from the Office of Biological and Environmental Research of the U.S. Department of Energy (DOE) Atmospheric System Research (ASR) program under Grant DE-SC0014294 and as part of the Atmospheric Radiation Measurement Climate Research Facility.

REFERENCES

Adirosi, E., L. Baldini, F. Lombardo, F. Russo, F. Napolitano, E. Volpi, and A. Tokay, 2015: Comparison of different fittings of drop spectra for rainfall retrievals. *Adv. Water Resour.*, **83**, 55–67, doi:10.1016/j.advwatres.2015.05.009.

Atlas, D., R. C. Srivastava, and R. S. Sekhon, 1973: Doppler radar characteristics of precipitation at vertical incidence. *Rev. Geophys.*, **11**, 1–35, doi:10.1029/RG011i001p00001.

Balsley, B. B., and K. S. Gage, 1982: On the use of radars for operational wind profiling. *Bull. Amer. Meteor. Soc.*, **63**, 1009–1018, doi:10.1175/1520-0477(1982)063<1009:OTUORF>2.0.CO;2.

Bartholomew, M. J., 2011: Two-dimensional video disdrometer (2DVD). Atmospheric Radiation Measurement (ARM) Climate Research Facility Data Archive, accessed 15 January 2015, doi:10.5439/1073032.

Beard, K. V., 1985: Simple altitude adjustments to raindrop velocities for Doppler radar analysis. *J. Atmos. Oceanic Technol.*, **2**, 468–471, doi:10.1175/1520-0426(1985)002<0468:SAATRV>2.0.CO;2.

Brandes, E. A., G. Zhang, and J. Vivekanandan, 2002: Experiments in rainfall estimation with a polarimetric radar in a subtropical environment. *J. Appl. Meteor.*, **41**, 674–685, doi:10.1175/1520-0450(2002)041<0674:EIREWA>2.0.CO;2.

Bringi, V. N., V. Chandrasekar, J. Hubbert, E. Gorgucci, W. L. Randeu, and M. Schoenhuber, 2003: Raindrop size distribution in different climate regimes from disdrometer and dual-polarized radar analysis. *J. Atmos. Sci.*, **60**, 354–365, doi:10.1175/1520-0469(2003)060<0354:RSDIDC>2.0.CO;2.

——, L. Tolstoy, M. Thurai, and W. A. Petersen, 2015: Estimation of spatial correlation of drop size distribution parameters and rain rate using NASA's S-band polarimetric radar and 2D video disdrometer network: Two case studies from MC3E. *J. Hydrometeor.*, **16**, 1207–1221, doi:10.1175/JHM-D-14-0204.1.

Chandrasekar, V., W. Li, and B. Zafar, 2005: Estimation of raindrop size distribution from spaceborne radar observations. *IEEE Trans. Geosci. Remote Sens.*, **43**, 1078–1086, doi:10.1109/TGRS.2005.846130.

Doviak, R. J., and D. S. Zrnić, 1993: *Doppler Radar and Weather Observations*. Academic Press, 562 pp.

Ecklund, W. L., K. S. Gage, and C. R. Williams, 1995: Tropical precipitation studies using a 915-MHz wind profiler. *Radio Sci.*, **30**, 1055–1064, doi:10.1029/95RS00640.

Ekerete, K.-M. E., F. H. Hunt, J. L. Jeffery, and I. E. Otung, 2015: Modeling rainfall drop size distribution in southern England using a Gaussian Mixture Model. *Radio Sci.*, **50**, 876–885, doi:10.1002/2015RS005674.

Fang, M., R. J. Doviak, and B. A. Albrecht, 2012: Analytical expressions for Doppler spectra of scatter from hydrometeors observed with a vertically directed radar beam. *J. Atmos. Oceanic Technol.*, **29**, 500–509, doi:10.1175/JTECH-D-11-00005.1.

Fukao, S., K. Wakasugi, T. Sato, S. Morimoto, T. Tsuda, I. Hirota, I. Kimura, and S. Kato, 1985: Direct measurement of air and precipitation particle motion by VHF Doppler radar. *Nature*, **316**, 712–714, doi:10.1038/316712a0.

Gage, K. S., 1990: Radar observation of the free atmosphere: Structure and dynamics. *Radar in Meteorology: Battan Memorial and 40th Anniversary Radar Meteorology Conference*, D. Atlas, Ed., Amer. Meteor. Soc., 534–565, doi:10.1007/978-1-935704-15-7_37.

Gossard, E. E., 1994: Measurement of cloud droplet size spectra by Doppler radar. *J. Atmos. Oceanic Technol.*, **11**, 712–726, doi:10.1175/1520-0426(1994)011<0712:MOCDSS>2.0.CO;2.

Hildebrand, P. H., and R. S. Sekhon, 1974: Objective determination of the noise level in Doppler spectra. *J. Appl. Meteor.*, **13**, 808–811, doi:10.1175/1520-0450(1974)013<0808:ODOTNL>2.0.CO;2.

Hou, A. Y., and Coauthors, 2014: The Global Precipitation Measurement Mission. *Bull. Amer. Meteor. Soc.*, **95**, 701–722, doi:10.1175/BAMS-D-13-00164.1.

Ignaccolo, M., and C. De Michele, 2014: Phase space parameterization of rain: The inadequacy of gamma distribution. *J. Appl. Meteor. Climatol.*, **53**, 548–562, doi:10.1175/JAMC-D-13-050.1.

Illingworth, A. J., and T. M. Blackman, 2002: The need to represent raindrop size spectra as normalized gamma distributions for the interpretation of polarization radar observations. *J. Appl. Meteor.*, **41**, 286–297, doi:10.1175/1520-0450(2002)041<0286:TNTRRS>2.0.CO;2.

Jensen, M. P., and Coauthors, 2015: The Midlatitude Continental Convective Clouds Experiment (MC3E) sounding network: Operations, processing and analysis. *Atmos. Meas. Tech.*, **8**, 421–434, doi:10.5194/amtd-7-9275-2014.

——, and Coauthors, 2016: The Midlatitude Continental Convective Clouds Experiment (MC3E). *Bull. Amer. Meteor. Soc.*, doi:10.1175/BAMS-D-14-00228.1, in press.

Kanofsky, L., and P. Chilson, 2008: An analysis of errors in drop size distribution retrievals and rain bulk parameters with a UHF wind profiling radar and a two-dimensional video disdrometer. *J. Atmos. Oceanic Technol.*, **25**, 2282–2292, doi:10.1175/2008JTECHA1061.1.

Kumjian, M. R., and O. P. Prat, 2014: The impact of raindrop collisional processes on the polarimetric radar variables. *J. Atmos. Sci.*, **8**, 3052–3067, doi:10.1175/JAS-D-13-0357.1.

Lhermitte, R., 1990: Attenuation and scattering of millimeter wavelength radiation by clouds and precipitation. *J. Atmos. Oceanic Technol.*, **7**, 464–479, doi:10.1175/1520-0426(1990)007<0464:AASOMW>2.0.CO;2.

Mather, J., and J. Voyles, 2013: The ARM Climate Research Facility: A review of structure and capabilities. *Bull. Amer. Meteor. Soc.*, **94**, 377–392, doi:10.1175/BAMS-D-11-00218.1.

Meneghini, R., S. W. Bidwell, L. Liao, R. Rincon, and G. M. Heymsfield, 2003: Differential-frequency Doppler weather radar: Theory and experiment. *Radio Sci.*, **38**, 8040, doi:10.1029/2002RS002656.

Morrison, H., S. A. Tessendorf, K. Ikeda, and G. Thompson, 2012: Sensitivity of a simulated midlatitude squall line to parameterization of raindrop breakup. *Mon. Wea. Rev.*, **140**, 2437–2460, doi:10.1175/MWR-D-11-00283.1.

Rajopadhyaya, D. K., P. T. May, R. C. Cifelli, S. K. Avery, C. R. Williams, W. L. Ecklund, and K. S. Gage, 1998: The effect of vertical air motions on rain rates and median volume diameter determined from combined UHF and VHF wind profiler measurements and comparisons with rain gauge measurements.

J. Atmos. Oceanic Technol., **15**, 1306–1319, doi:10.1175/1520-0426(1998)015<1306:TEOVAM>2.0.CO;2.

Seto, S., T. Iguchi, and T. Oki, 2013: The basic performance of a precipitation retrieval algorithm for the Global Precipitation Measurement Mission's single/dual-frequency radar measurements. *IEEE Trans. Geosci. Remote Sens.*, **51**, 5239–5251, doi:10.1109/TGRS.2012.2231686.

Steiner, M., J. A. Smith, and R. Uijlenhoet, 2004: A microphysical interpretation of radar reflectivity–rain rate relationships. *J. Atmos. Sci.*, **61**, 1114–1131, doi:10.1175/1520-0469(2004)061<1114:AMIORR>2.0.CO;2.

Tapiador, F. J., Z. S. Haddad, and J. Turk, 2014: A probabilistic view on raindrop size distribution modeling: A physical interpretation of rain microphysics. *J. Hydrometeor.*, **15**, 427–443, doi:10.1175/JHM-D-13-033.1.

Testud, J., S. Oury, R. A. Black, P. Amayenc, and X. K. Dou, 2001: The concept of "normalized" distribution to describe raindrop spectra: A tool for cloud physics and cloud remote sensing. *J. Appl. Meteor.*, **40**, 1118–1140, doi:10.1175/1520-0450(2001)040<1118:TCONDT>2.0.CO;2.

Thurai, M., V. N. Bringi, and P. T. May, 2010: CPOL radar-derived drop size distribution statistics of stratiform and convective rain from two regimes in Darwin, Australia. *J. Atmos. Oceanic Technol.*, **27**, 932–942, doi:10.1175/2010JTECHA1349.1.

Wakasugi, K., A. Mizutani, M. Matsuo, S. Fukao, and S. Kato, 1986: A direct method of deriving drop size distribution and vertical air velocities from VHF Doppler radar spectra. *J. Atmos. Oceanic Technol.*, **3**, 623–629, doi:10.1175/1520-0426(1986)003<0623:ADMFDD>2.0.CO;2.

——, ——, ——, ——, and ——, 1987: Further discussion on deriving drop-size distribution and vertical air velocities from VHF Doppler radar spectra. *J. Atmos. Oceanic Technol.*, **4**, 170–179, doi:10.1175/1520-0426(1987)004<0170:FDODDS>2.0.CO;2.

White, A. B., J. R. Jordan, B. E. Martner, F. M. Ralph, and B. W. Bartram, 2000: Extending the dynamic range of an S-band radar for cloud and precipitation studies. *J. Atmos. Oceanic Technol.*, **17**, 1226–1234, doi:10.1175/1520-0426(2000)017<1226:ETDROA>2.0.CO;2.

Williams, C. R., 2012a: Vertical air motion retrieved from dual-frequency profiler observations. *J. Atmos. Oceanic Technol.*, **29**, 1471–1480, doi:10.1175/JTECH-D-11-00176.1.

——, 2012b: S-band vertically pointing radar. Atmospheric Radiation Measurement (ARM) Climate Research Facility Data Archive, accessed 15 January 2015. [Available online at http://iop.archive.arm.gov/arm-iop/2011/sgp/mc3e/williams-s_band/.]

——, 2012c: 449-MHz vertically pointing radar. Atmospheric Radiation Measurement (ARM) Climate Research Facility Data Archive, accessed 15 January 2015. [Available online at http://iop.archive.arm.gov/arm-iop/2011/sgp/mc3e/williams-449_prof/.]

——, and K. S. Gage, 2009: Raindrop size distribution variability estimated using ensemble statistics. *Ann. Geophys.*, **27**, 555–567, doi:10.5194/angeo-27-555-2009.

——, A. B. White, K. S. Gage, and F. M. Ralph, 2007: Vertical structure of precipitation and related microphysics observed by NOAA profilers and TRMM during NAME 2004. *J. Climate*, **20**, 1693–1712, doi:10.1175/JCLI4102.1.

——, and Coauthors, 2014: Describing the shape of raindrop size distributions using uncorrelated raindrop mass spectrum parameters. *J. Appl. Meteor. Climatol.*, **53**, 1282–1296, doi:10.1175/JAMC-D-13-076.1.